A Multipurpose Study of BaZrS3 and BaHfS3: Absolute Entropies, Thermal Decomposition, and Prediction of Intrinsic and Extrinsic Thermodynamic Stability

THE JOURNAL OF PHYSICAL CHEMISTRY C
A JOURNAL OF THE AMERICAN CHEMICAL SOCIETY

pubs.acs.org/JPCC
Article

A Multipurpose Study of $BaZrS_3$ and $BaHfS_3$: Absolute Entropies, Thermal Decomposition, and Prediction of Intrinsic and Extrinsic Thermodynamic Stability

Alexis Gibson, Andrea Ciccioli,* Natalie Parkinson, Riccardo Testa, Corrado Di Conzo, Marco Rossi, Alessandro Latini, Stefano Vecchio Ciprioti, Hasan Arif Yetkin, Phillip J. Dale, Brian Woodfield,* and Lorenza Romagnoli*

Cite This: J. Phys. Chem. C 2026, 130, 7153−7166

ABSTRACT: Chalcogenide perovskites have emerged in the past few years as very promising candidates for photovoltaic applications. However, experimental studies on these materials are still relatively scarce and there is a concerning lack of experimentally determined physical properties, which is particularly serious for thermodynamic properties, notwithstanding their importance in the assessment of the suitability of these materials for the proposed applications. In this work, the thermodynamic properties of chalcogenide perovskites $BaZrS_3$ and $BaHfS_3$ were therefore studied with the aim of estimating the intrinsic stability of the two compounds and the thermodynamic tendency to react under relevant synthesis/real world environments. The measurement of heat capacities from 1.8 to 300 K was performed for the first time and absolute entropies of the two materials were derived therefrom. Furthermore, the thermal decomposition of $BaZrS_3$ was investigated by means of Knudsen effusion mass spectrometry up to 1850 K, revealing the release of gaseous sulfur as the only gaseous decomposition product up to about 1600 K. The largely dominant sulfur species were S(g) and S_2(g), as expected for a low sulfur-activity phase, with higher oligomers S_3−S_8 only observed in the very first steps of heating. Above 1600 K, also BaS(g) was identified in the vapor phase, with an activity lower than unity, suggesting that pure solid BaS is not formed upon thermal degradation. XRD, SEM, TEM and Raman analyses performed on the residual sample indicated the formation of the Ruddlesden−Popper phase Ba_2ZrS_4, confirming previous theoretical predictions. However, no isothermal invariance of the sulfur partial pressure was observed, making it impossible to identify any heterogeneous equilibrium established under the effusion conditions. Finally, by combining the newly determined absolute entropies of the two chalcogenide perovskites with theoretical formation energies available in the literature, the intrinsic thermodynamic stability of $BaZrS_3$ and $BaHfS_3$ and the thermodynamic degradation behavior under oxygen, water, and water + CO_2 gaseous atmospheres were predicted. Both $BaZrS_3$ and $BaHfS_3$ were shown to be stable with respect to the binary sulfides BaS, ZrS_2, and HfS_2 at room temperature, with the entropic term causing further stabilization at higher temperatures.

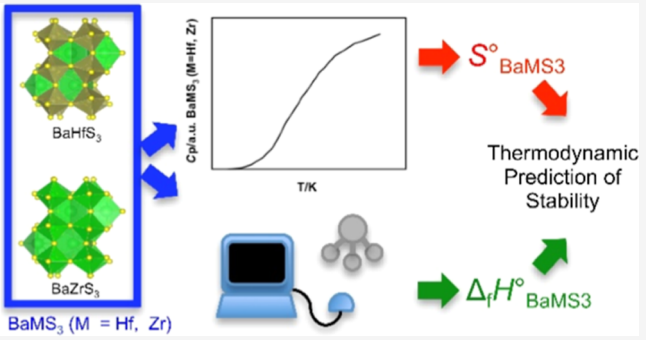

1. INTRODUCTION

Starting from the work published in 2015 by Sun et al.,[1] in which chalcogenide perovskites $ABCh_3$ (Ch = group VI divalent anion) were proposed for photovoltaic applications, based on their band gaps and optical absorption properties, this class of inorganic semiconductors has gained an ever-increasing attention as a potential alternative to metal halide hybrid perovskites for the top cell in the tandem application.[2] In fact, while the latter type of materials, whose prototypical compound is methylammonium lead triiodide, has reached, in less than two decades, excellent photovoltaic performances on a laboratory and industrial scale, they also, unfortunately, revealed almost immediately serious drawbacks to their commercialization, mainly due to the lack of thermal and chemical stability.[3]

The potential for optoelectronic and other functional applications of ABO_3 crystalline materials with perovskite structure had been already recognized previously.[4] Indeed, oxide perovskites constitute a widely investigated class of

Received: February 16, 2026
Revised: April 29, 2026
Accepted: April 29, 2026
Published: May 8, 2026

https://doi.org/10.1021/acs.jpcc.6c01064
J. Phys. Chem. C 2026, 130, 7153−7166

Table 1. Experimental Structural and Electronic Properties of $BaZrS_3$ and $BaHfS_3$

material	space group	a/Å	b/Å	c/Å	Unit cell volume/Å^3	Band gap/eV
$BaZrS_3$	*Pnma*	7.0599[a]	9.9813[a]	7.0251[a]	495.0376[a]	1.75−1.94[b]
$BaHfS_3$	*Pnma*	7.0020[a]	9.9150[a]	6.9950[a]	485.6267[a]	2.06−2.17[b]

[a]Data are taken from ref 11. [b]The complete set of values can be found in ref 2.

materials: their multifarious properties, such as ferroelectricity, ferromagnetism, thermal conductivity and superconductivity, have been known for decades,[5] and practical applications as catalysts[6,7] were also reported. In addition, their thermal and chemical stability are desirable characteristics in view of long-term utilization. Regretfully, the band gap values of oxide perovskites, in most cases above 3 eV, are too large to allow efficient solar light harvesting for photovoltaic applications, the optimal value for maximum photo conversion efficiency being around 1.34 eV, according to the Shockley−Queisser limit.[8]

However, the optoelectronic properties of chalcogenide perovskites containing anions other than oxide have received practically no attention until the publication of the aforementioned paper by Sun et al.,[1] although the earliest reported synthesis and structure determination of $BaZrS_3$, $BaTiS_3$ and $SrTiS_3$ ternary sulfides date back to 1957,[9] and a few other compounds of this class were prepared and crystallographically characterized subsequently.[10,11] Among the reasons which hindered the study of these materials, there are the very demanding conditions needed for their preparation, in terms of high temperatures and toxic reagents.[2] Despite the notable improvements achieved in very recent years in the synthesis methodologies for the attainment of both powders and thin films,[12] as a matter of fact, most of the research work on this class of materials is carried out by means of first-principles calculations[13−15] and many of their fundamental properties have never been experimentally determined.

Table 1 summarizes the most important structural and electronic characteristics measured for $BaZrS_3$ and $BaHfS_3$, two of the most investigated chalcogenide perovskites and the subject of the present study.

The lack of experimentally determined properties is especially true for thermodynamic properties. While the formation energy from binary precursors of a number of chalcogenide perovskites has been calculated by means of DFT by several groups[14−20] and is also reported in online repositories, such as the Materials Project[21] and Open Quantum Materials Database,[22,23] no experimental formation energy values have been reported so far. Furthermore, in all these studies only perovskite stability with respect to binary precursors is predicted, whereas competing formation or decomposition reactions are not considered, and entropy contributions are usually neglected. An interesting approach has been recently used in the work by Kayastha et al.,[24] where also the Gibbs energy changes for decomposition of $BaZrS_3$ into ZrS_2 and competing 2D Ruddlesden−Popper phases $Ba_{n+1}Zr_nS_{3n+1}$ (with n = 1, 2, 3) were evaluated, by using an ab initio thermodynamic model previously applied to Cu_2ZnSnS_4 (CZTS).[25] Subsequently, by the same approach, this group predicted the Gibbs free energy of formation of $BaZrS_3$, both from the elements in the solid state and from binary precursors, and also studied the effect of sulfur vapor pressure on the formation of the perovskite, of different binary reaction intermediates and of competing phases.[26]

The experimental assessment of the thermal stability of chalcogenide perovskites and the measurement of their thermodynamic properties is crucial to test the accuracy of computational models, and also to provide helpful information on viable conditions for thin film deposition, which is essential for real applications. In this regard, we report the determination of thermodynamic functions of two of the most promising chalcogenide perovskites, namely $BaZrS_3$ and $BaHfS_3$, from low temperature heat capacity measurements, in the present work. On this basis, the intrinsic and extrinsic thermodynamic stability of these materials in different environmental conditions was evaluated. Additionally, thermal decomposition of $BaZrS_3$ was studied for the first time by the Knudsen effusion mass spectrometry (KEMS) technique, which allowed the identification of gaseous species released at high temperature and the measurement of their partial pressures.

2. METHODS

2.1. Synthesis of $BaZrS_3$ and $BaHfS_3$

All the reagents were used as received. Barium sulfide powder (99.9% purity), hafnium powder 325 mesh (99.5% purity excluding 2−4% Zr), sulfur powder (99.98% purity) and toluene (ACS-ISO grade) were purchased from Sigma-Aldrich-Merck. Zirconium powder 60−100 mesh (99.8% purity) was purchased from Chempur. Wheaton 10 mL prescored clear borosilicate glass ampules were purchased from Sigma-Aldrich-Merck. Materials were prepared according to a previously published procedure.[27,28] BaS, Zr or Hf, and S were ground in a 1:1:3 ratio in an agate mortar for 20 min, then the mixture was transferred to a glass ampule, previously dried in an oven at 150 °C, and evacuated by a rotary pump to $3\cdot10^{-1}$ mbar, while heating to about 80 °C by a blow dryer. The ampule connected to the vacuum pump was flame-sealed with a butane torch, inserted in an alumina crucible and annealed in a muffle furnace heated at 500 °C for 16 h. Subsequently, the crucible with the ampule was taken out, while still at 500 °C, let cool down to room temperature, then the ampule was opened, the product recovered and ground in an agate mortar, washed with cold water, filtered under suction, washed three times with small amounts of acetone and dried. If excess sulfur is present, the solid is transferred in a beaker and stirred for 1 h in toluene at 85 °C to remove the elemental sulfur, filtered under suction and dried in air. X-ray diffraction patterns (Figure S1a,b) of the so obtained powders (black for $BaZrS_3$ and red for $BaHfS_3$) confirmed the purity of products.

2.2. Powder X-ray Diffraction

Diffraction patterns of the as-synthesized $BaZrS_3$ and $BaHfS_3$ and of the solid residue left after KEMS experiments on $BaZrS_3$ were acquired with a Malvern Panalytical X'Pert Pro MPD diffractometer (Cu Kα radiation, λ = 1.54184 Å), operating in Bragg−Brentano geometry and equipped with an ultrafast X'Celerator RTMS detector. The angular range 2θ = 10−90° was used in all the measurements.

2.3. Thermogravimetry-Differential Thermal Analysis

Simultaneous TG-DTA on $BaZrS_3$ and $BaHfS_3$ were carried out with a Netzsch STA409 PC Luxx thermal analyzer, in flowing Ar atmosphere (100 cm$^3\cdot$min^{-1} @STP, purity >99.9995%) with a heating rate of 10 K$\cdot$min^{-1} from room temperature to 600 °C, using alumina crucibles. Thermograms were recorded for the as-such synthesized samples and after a treatment in high vacuum up to about

https://doi.org/10.1021/acs.jpcc.6c01064
J. Phys. Chem. C 2026, 130, 7153−7166

330 °C, performed on the samples destined for heat capacity measurements.

2.4. Raman Spectroscopy

Raman measurements have been performed at room temperature at various spots on the solid residue obtained after KEMS experiments on $BaZrS_3$, using a Renishaw inVia Reflex Raman Microscope configured in backscattering geometry. The powder sample was placed into the openings of a 100-mesh copper grid, which was affixed to double-sided carbon tape, ensuring that the powder sticked to the carbon tape. All Raman spectra were acquired using a 50× objective with two different excitation wavelengths: 633 nm (grating: 2400 L/mm) and 785 nm (grating: 1200 lines/mm). Furthermore, a silicon wafer as a calibration sample was used to calibrate each laser wavelength. In order to exclude any laser-induced damage on the sample, visual inspections were done on each measurement spot before and after each measurement. All obtained Raman spectra were normalized to 1 according to highest intensity.

2.5. Heat Capacity Measurements

Heat capacity measurements were performed on a Quantum Design Physical Property Measurement System (PPMS) in zero magnetic field from 1.8 to 300 K. The samples were prepared according to a method devised for measuring the heat capacities of insulating powders.[29,30] Samples were enclosed in copper cups (0.025 mm thick, 99.999% purity from Alfa Aesar) with two small copper coils of the same purity inserted in each cup to ensure uniform heating throughout the samples. After being pressed into a pellet, the sample was attached to the sample holder using a small amount of Apiezon N grease and placed in the PPMS. An addenda measurement was performed before the measurement to account for the heat capacity of the sample holder and the grease. This method has an estimated accuracy of ±2% below 10 K and ±1% from 10 to 300 K. The sample and copper masses used are listed in Table 2.

Table 2. Details of the PPMS Calorimetric Measurements Including Pressures (p), Sample Mass (M_s), and Copper Mass (M_{Cu})[a]

	p/mPa	M_s/mg	M_{Cu}/mg
$BaHfS_3$	1.2	9.18	22.97
$BaZrS_3$	1.2	10.64	21.07

[a]The estimated standard uncertainties in the masses $M_{s,Cu}$ and pressures p are $u(M_{s,Cu})$ = 0.06 mg and $u(p)$ = 0.1 mPa.

2.6. Knudsen Effusion Mass Spectrometry

KEMS experiments were carried out on $BaZrS_3$, synthesized according to the procedure detailed previously, with a single focusing 90° magnetic sector mass spectrometer, originally manufactured by Patco, equipped with a Knudsen molecular source, as described in.[31] The sample was placed in a tungsten effusion cell, provided with a lid with a small orifice (0.95 mm diameter), enclosed in an external tantalum crucible. A spiral-shaped tungsten heating element surrounding the crucible was used. The crucible and the heating coil were in turn surrounded by several thermal shields made of tantalum foil. Ultrahigh vacuum is produced in the apparatus (typical residual pressure in the ion source region: $5{\cdot}10^{-7}$ mbar) by a turbomolecular and three ion pumps. The temperature was measured by a W5% Re–W26% Re (type C) thermocouple, inserted in a small hole drilled in the bottom of the external crucible. Ionization efficiency curves were measured for all the detected ions and appearance energies (i.e., the lowest value of the electron energy necessary to produce an ion) were determined with the vanishing current method, by correcting the observed values based on the appearance energy of the ion Au^+, taken as reference.[32] Ba-containing ions also showed some thermal contribution (i.e., they were produced by heating and not only by electron impact), which was assessed by switching off the electron-emitting filament and subtracted to total intensity for partial pressure calculations (see eq 1 below). The energy of the ionizing electrons used was adjusted based on the maximum ionization efficiency and was between 8 and 20 eV. A movable shutter is placed between the molecular source and the spectrometer, allowing one to distinguish ions from the Knudsen cell from background species. Ion intensities were taken as the difference between total intensities and those measured with the shutter shifted so as to exclude the ions from the cell. Partial pressures P_i of species i in the gas phase were obtained by applying eq 1

$$P_i = \frac{k_{\mathrm{instr}}}{\sigma_i} \sum_k \frac{I_k^+ T \sqrt{M_k}}{a_k} \tag{1}$$

In this equation, I_k^+ are ion currents of ions k (which can be either molecular ions or fragments) produced from neutral species i upon electron impact, M_k is their molecular mass, a_k the isotope abundance of the monitored isotope of k, T is the absolute temperature, σ_i is the ionization cross section of i, and k_{instr} is an instrumental constant, whose value is given by $\frac{P_{\mathrm{ref}} a_{\mathrm{ref}} \sigma_{\mathrm{ref}}}{I_{\mathrm{ref}}^+ \sqrt{M_{\mathrm{ref}}} T_{\mathrm{ref}}}$, derived from calibration experiments with a reference substance of known vapor pressure P_{ref}. In the experiments described in this work, calibration was carried out by vaporizing Au (99.99% purity), supplied by Engelhard, and Ag (purity 99.999%), supplied by Alfa Aesar. Sulfur activity in the perovskite was estimated by the equation

$$a_S = \sqrt[m-n]{\frac{p_{S_m}}{p_{S_n}}} \tag{2}$$

where S_m and S_n are two oligomers formed in the gas phase.

As discussed in Section 3.2, a KEMS experiment was also carried out, for the sake of comparison, on pure BaS, under the same experimental conditions used for $BaZrS_3$.

2.7. Transmission and Scanning Electron Microscopy

TEM analysis was performed on pristine $BaZrS_3$ and the residue after KEMS experiments. Each sample was prepared by dispersing 3 mg of powder in 8 mL of hexane, sonicating for 40 min, and depositing a few drops of this dispersion onto a TEM grid. Measurements were performed with an F200 JEOL Multipurpose transmission electron microscope equipped with a GATAN Rio16 CMOS camera and a JEOL EDX spectrometer.[33] Electron diffraction patterns were indexed using CrysTBox software with the DiffractGUI tool.[34] SEM images of both powdered samples were acquired using a Thermo Fisher Phenom ProX equipped with an EDX spectrometer for compositional analysis.

2.8. Thermodynamic Calculations

Simulations aimed at predicting the thermodynamic stability of $BaZrS_3$ under various reactive atmospheres (see Section 3.3) were carried out using the POLY-3 module (a software for equilibrium calculations based on a Gibbs energy minimization algorithm) of the Thermo-Calc package, version L.[35] To this end, a user database was assembled by extracting the thermodynamic data retrieved in the SGTE Substance database SSUB94[36] and by adding the Gibbs energy function $G(T)-H_{SER}(298)$ for the $BaZrS_3$ phase as given by the following expressions: $-1102175 + 11.748{\cdot}T - 0.3338{\cdot}T^2 - 0.00025653{\cdot}T^3 + 8.138{\cdot}10^{-7}{\cdot}T^4$ up to 298.15 K and $-1071922.6 - 166.93{\cdot}T - 0.069449{\cdot}T^2$ from 298.15 to 500 K. The first equation was obtained by a simplified fit of the data measured in the present work, whereas the high temperature equation was estimated by using for the enthalpy of formation from the elements at 298.15 K the value −1077 $kJ{\cdot}mol^{-1}$ (see Section 3.3 and eq 13 therein) and by approximating the heat content and entropy functions at T > 298.15 K by the additivity rule $C_p(BaZrS_3) = C_p(BaS) + C_p(ZrS_2)$ corrected by a term accounting for the difference with our experimental values at 298.15 K. The other solid phases included in the database are the following: $BaCO_3$, BaC_2, $Ba(OH)_2$, BaH_2, BaO, BaO_2, $BaZrO_3$, $BaSO_4$, BaS, Ba, ZrC, C (graphite), C (diamond), ZrO_2, ZrS_2, Zr_2S_3, S, Zr.

https://doi.org/10.1021/acs.jpcc.6c01064
J. Phys. Chem. C 2026, 130, 7153−7166

3. RESULTS AND DISCUSSION

3.1. Heat Capacities and Thermodynamic Functions of $BaZrS_3$ and $BaHfS_3$

Heat capacity measurements were carried out on samples that had been previously heated up to 600 K in high vacuum for about 4 h to remove any possible residual excess sulfur. TG-DTA measurements were performed under inert atmosphere before and after the treatment. The thermograms, reported as Figure S2a,b, indicate that the treatment successfully removed the volatile sample impurities; X-ray diffraction patterns confirmed that no phase change occurred during heating.

The measured heat capacities for each sample are listed in Tables S1 and S2. Figure 1 shows the measured heat capacities

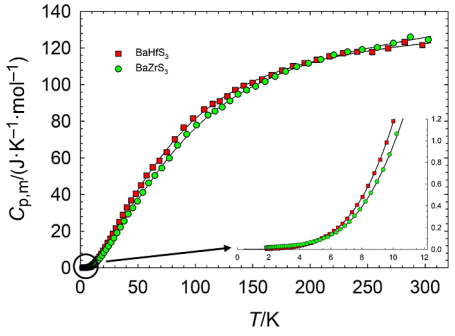

Figure 1. Measured molar heat capacity as a function of temperature for $BaHfS_3$ and $BaZrS_3$. The black curve placed behind the heat capacity is a plot of the theoretical fits in Table 3. The inset shows the points at $T < 10$ K. The point removed due to error in the heat capacity of grease at high temperatures is included in the plot of the raw data for $BaHfS_3$, but is not included as part of the data used in the calculation of the theoretical fits.

for each sample with their theoretical fits and Figure S3 shows the data's deviations from the fits based on Table 3. The heat capacity data were fitted using theoretical functions in two distinct temperature regions ($T < 10$ K and $T > 40$ K). An orthogonal polynomial was used to smoothly transition between the two regions. Fitting parameters are given in Table 3, and thermodynamic functions at smoothed temperatures based on the fits are given in Tables 4 and 5.

Variations in the high temperature data points are believed to be caused by uncertainty in the heat capacity of the Apiezon N grease at high temperatures.[29] To correct for this problem, one of the high temperature data points for $BaHfS_3$ was removed from the data when calculating the theoretical fits for this region.

The heat capacity of the $BaHfS_3$ and $BaZrS_3$ samples are represented below 10 K by

$$C_{p,m} = B_{-3}T^{-3} + B_{-2}T^{-2} + B_3T^3 + B_5T^5 + B_7T^7 \quad (3)$$

where B_{-3}, B_{-2}, B_3, B_5, and B_7 are constants obtained from fitting the data. The B_3T^3,B_5T^5, and B_7T^7 terms represent the lattice contribution to the heat capacity and account for any anharmonicity in lattice phonons.[37] The B_{-3} and B_{-2} terms are taken as the first two terms in the series expansion of the low-temperature limit of a Schottky anomaly, commonly found in compounds with a nuclear hyperfine field.[37,38] The B_{-3} and B_{-2} terms were excluded when calculating the thermodynamic functions to focus on chemical contributions.

Table 3. Parameters for Low$T$ (<10 K), mid T (5 K < T < 65 K), and High$T$ (T > 40 K) Fits of Heat Capacity Data (in J·K^{-1}·mol^{-1}) for $BaHfS_3$ and $BaZrS_3$[a]

	Parameter	$BaHfS_3$	$BaZrS_3$
Low T Fits	B_{-3}/J·K^2·mol^{-1}	−0.07618	−0.39307
	B_{-2}/J·K·mol^{-1}	0.04514	0.25762
	B_3/J·K^{-4}·mol^{-1}	$2.8704\cdot10^{-4}$	$4.5928\cdot10^{-4}$
	B_5/J·K^{-6}·mol^{-1}	$1.2574\cdot10^{-5}$	$2.5424\cdot10^{-6}$
	B_7/J·K^{-8}·mol^{-1}	$-3.9500\cdot10^{-8}$	$2.8626\cdot10^{-8}$
	% RMS	1.86	2.70
	Range/K	1.87−8.29	1.85−6.75
Mid T Fits	A_0/J·K^{-1}·mol^{-1}	−1.7753	−1.4612
	A_1/J·K^{-2}·mol^{-1}	1.1430	0.95464
	A_2/J·K^{-3}·mol^{-1}	−0.28108	−0.23555
	A_3/J·K^{-4}·mol^{-1}	0.033108	0.027779
	A_4/J·K^{-5}·mol^{-1}	$-1.8195\cdot10^{-3}$	$-1.5348\cdot10^{-3}$
	A_5/J·K^{-6}·mol^{-1}	$5.6048\cdot10^{-5}$	$4.7571\cdot10^{-5}$
	A_6/J·K^{-7}·mol^{-1}	$-9.8874\cdot10^{-7}$	$-8.4268\cdot10^{-7}$
	A_7/J·K^{-8}·mol^{-1}	$9.3047\cdot10^{-9}$	$7.9411\cdot10^{-9}$
	A_8/J·K^{-9}·mol^{-1}	$-3.6153\cdot10^{-11}$	$-3.0814\cdot10^{-11}$
	% RMS	0.52	0.91
	Range/K	8.29−53.48	6.75−45.08
High T Fits	B/J·K^{-2}·mol^{-1}	0.026567	0.056394
	m/mol	2.3399	2.2448
	Θ_D/K	155.77	178.38
	n/mol	2.5259	2.4296
	Θ_E/K	332.62	359.31
	% RMS	0.95	0.91
	Range/K	53.48−297.56	45.08−302.75

[a]One Point was Excluded in the High-Temperature Fits of $BaHfS_3$.

The middle temperature regions were fitted to eighth order orthogonal polynomials, which do not have a theoretical basis but are used to provide a smooth overlap between the low and high temperature functions[39]

$$C_{p,m} = \sum_{i=0}^{8} A_i T^i \quad (4)$$

Heat capacity data in the high temperature region ($T > 40$ K) were fitted with a combination of Debye and Einstein functions, which represent the contribution of lattice vibrations at higher temperatures

$$C_{p,m} = BT + m\cdot D(\Theta_D/T) + n\cdot E(\theta_E/T) \quad (5)$$

where $D(\Theta_D/T)$ is a Debye function and $E(\Theta_E/T)$ is an Einstein function, and m and n represent the number of Debye or Einstein oscillators with characteristic temperatures of Θ_D and Θ_E respectively.[39] The B term is used to correct for the difference in isochoric and isobaric heat capacities.[40]

3.2. Thermal Decomposition of $BaZrS_3$ Studied by Knudsen Effusion Mass Spectrometry

Vaporization of $BaZrS_3$ by Knudsen effusion mass spectrometry was undertaken with the main aim to ascertain the nature of the vapor phase released from this compound at high temperature under close-to-equilibrium conditions, thus getting information on the thermodynamic prerequisites for possible vapor deposition processes of thin films.

Three consecutive experiments were carried out on the same $BaZrS_3$ sample. In the first experiment, the sample was mildly heated, up to $T = 462$ K, and only ions formed from sulfur oligomers up to S_8^+ (with prevalence of S_2^+ and S^+, the latter

https://doi.org/10.1021/acs.jpcc.6c01064
J. Phys. Chem. C 2026, 130, 7153−7166

Table 4. Standard Thermodynamic Functions of $BaHfS_3$[b]

T/K	$C_{p,m}$/J·K·mol^{-1}	$\Delta_{0K}{}^{T}S_m°$/J·K·mol^{-1}	$\Delta_{0K}{}^{T}H_m°$/kJ·mol^{-1}	$\Phi m°$[a]/J·K·mol^{-1}
0	0	0	0	0
2	$4.457\cdot10^{-3}$	$8.452\cdot10^{-4}$	$1.281\cdot10^{-6}$	$2.047\cdot10^{-4}$
3	0.01291	$3.182\cdot10^{-3}$	$7.308\cdot10^{-6}$	$7.462\cdot10^{-4}$
4	0.03223	$8.606\cdot10^{-3}$	$2.663\cdot10^{-5}$	$1.949\cdot10^{-3}$
5	0.07329	0.01938	$7.567\cdot10^{-5}$	$4.245\cdot10^{-3}$
6	0.14962	0.03864	$1.825\cdot10^{-4}$	$8.229\cdot10^{-3}$
7	0.27796	0.07044	$3.904\cdot10^{-4}$	0.01467
8	0.47672	0.11956	$7.605\cdot10^{-4}$	0.02450
9	0.76957	0.19155	$1.375\cdot10^{-3}$	0.03882
10	1.1656	0.29222	$2.334\cdot10^{-3}$	0.05887
15	4.5514	1.3331	0.01574	0.28391
20	9.4587	3.2922	0.05038	0.77340
25	14.930	5.9850	0.11122	1.5361
30	20.627	9.2077	0.20003	2.5399
35	26.476	12.826	0.31776	3.7468
40	32.236	16.740	0.46466	5.1237
45	37.546	20.849	0.63935	6.6414
50	42.393	25.058	0.83930	8.2721
60	51.836	33.636	1.3112	11.782
70	60.490	42.286	1.8735	15.522
80	68.351	50.886	2.5184	19.406
90	75.339	59.349	3.2376	23.376
100	81.459	67.611	4.0223	27.388
110	86.773	75.630	4.8641	31.411
120	91.370	83.382	5.7553	35.421
130	95.348	90.856	6.6894	39.399
140	98.798	98.052	7.6605	43.334
150	101.80	104.97	8.6639	47.214
160	104.43	111.63	9.6953	51.033
170	106.74	118.03	10.751	54.787
180	108.79	124.19	11.829	58.473
190	110.61	130.12	12.926	62.089
200	112.24	135.84	14.041	65.634
210	113.70	141.35	15.171	69.109
220	115.03	146.67	16.314	72.514
230	116.24	151.81	17.471	75.851
240	117.35	156.78	18.639	79.120
250	118.37	161.59	19.818	82.323
260	119.31	166.25	21.006	85.462
270	120.19	170.77	22.204	88.539
273.15	120.45	172.17	22.583	89.495
280	121.00	175.16	23.409	91.554
290	121.77	179.42	24.623	94.511
298.15	122.36	182.80	25.618	96.878
300	122.49	183.56	25.845	97.411

[a]$\Phi_m° = \Delta_{0K}^{T}S_m° - \frac{\Delta_{0K}^{T}H_m°}{T}$ [b]All calculated thermodynamic values have an estimated standard uncertainty of 0.02 X below 10 K and 0.01 X at and above 10 K, where X represents the thermodynamic property. $C_{p,m}$, $\Delta_{0K}{}^{T}S_m°$, $\Delta_{0K}{}^{T}H_m°$, and $\Phi_m°$ are the heat capacity, standard entropy, standard enthalpy, and Gibbs function, respectively. Nuclear contributions were excluded when calculating thermodynamic functions. Values are reported with extended significant digits to preserve the original measurement precision and facilitate future data fitting and modeling.

being, at least in part, a fragment of $S_2(g)$) were detected in the mass spectrum of the perovskite. The values of sulfur activities (Figure S4), being in the range 0.1−0.8 in the first stage of the measurement and rapidly dropping to ~10^{-17} after 2 h of heating (with disappearing of all oligomers higher than S_2), indicate the initial presence of minimal amounts of excess sulfur impurities from the synthesis, under the detection limit of PXRD.

The subsequent experiments have been performed at higher temperatures, up to 1294 K for the second run and up to 1852 K for the third. By increasing temperature, a change in the composition of the vapor was observed. Sulfur was found exclusively in the form of monomer and dimer, S(g) and S_2(g), and also Ba-containing molecules started to be released from temperatures around 1600 K. As an instance, the spectrum of the gas phase produced from $BaZrS_3$ at 1829 K is shown in Figure 2.

Figure 2 shows the presence of the ion species S^+, S_2^+, Ba^+, BaS^+ and $Ba_2S_2^+$ (the latter with a very low intensity), while no Zr-containing species were detected in the gas phase. This

https://doi.org/10.1021/acs.jpcc.6c01064
J. Phys. Chem. C 2026, 130, 7153−7166

Table 5. Standard Thermodynamic Functions of $BaZrS_3$[b]

T/K	$C_{p,m}$/J·K·mol^{-1}	$\Delta_{0K}{}^{T}S_m^\circ$/J·K·mol^{-1}	$\Delta_{0K}{}^{T}H_m^\circ$/kJ·mol^{-1}	Φ_m°[a]/J·K·mol^{-1}
0	0	0	0	0
2	0.01903	$1.242\cdot10^{-3}$	$1.865\cdot10^{-6}$	$3.090\cdot10^{-4}$
3	0.02715	$4.266\cdot10^{-3}$	$9.633\cdot10^{-6}$	$1.055\cdot10^{-3}$
4	0.04243	0.01039	$3.136\cdot10^{-5}$	$2.545\cdot10^{-3}$
5	0.07475	0.02105	$7.978\cdot10^{-5}$	$5.089\cdot10^{-3}$
6	0.13232	0.03817	$1.746\cdot10^{-4}$	$9.069\cdot10^{-3}$
7	0.22936	0.06460	$3.474\cdot10^{-4}$	0.01498
8	0.39126	0.10500	$6.517\cdot10^{-4}$	0.02354
9	0.63017	0.16408	$1.156\cdot10^{-3}$	0.03567
10	0.95227	0.24641	$1.940\cdot10^{-3}$	0.05242
15	3.7191	1.0965	0.01289	0.23733
20	7.7506	2.6994	0.04123	0.63792
25	12.306	4.9120	0.09123	1.2628
30	17.164	7.5806	0.16478	2.0878
35	22.291	10.609	0.26334	3.0850
40	27.465	13.925	0.38778	4.2301
45	32.329	17.445	0.53745	5.5014
50	37.102	21.099	0.71108	6.8774
60	46.223	28.678	1.1282	9.8754
70	54.797	36.455	1.6337	13.115
80	62.737	44.298	2.2220	16.523
90	69.951	52.111	2.8860	20.044
100	76.408	59.822	3.6185	23.637
110	82.132	67.378	4.4118	27.271
120	87.183	74.746	5.2589	30.922
130	91.636	81.904	6.1534	34.570
140	95.568	88.842	7.0898	38.200
150	99.051	95.556	8.0633	41.801
160	102.15	102.05	9.0696	45.365
170	104.93	108.33	10.105	48.885
180	107.42	114.40	11.167	52.357
190	109.68	120.27	12.253	55.777
200	111.74	125.95	13.360	59.145
210	113.62	131.44	14.487	62.457
220	115.36	136.77	15.632	65.715
230	116.96	141.93	16.794	68.917
240	118.46	146.94	17.971	72.064
250	119.86	151.81	19.163	75.157
260	121.17	156.53	20.368	78.196
270	122.42	161.13	21.586	81.183
273.15	122.79	162.55	21.972	82.113
280	123.59	165.60	22.816	84.119
290	124.71	169.96	24.058	87.004
298.15	125.59	173.43	25.078	89.319
300	125.78	174.21	25.310	89.840

[a]$\Phi_m^\circ = \Delta_{0K}^{T}S_m^\circ - \frac{\Delta_{0K}^{T}H_m^\circ}{T}$ [b]All calculated thermodynamic values have an estimated standard uncertainty of 0.02 X below 10 K and 0.01 X at and above 10 K, where X represents the thermodynamic property. $C_{p,m}$, $\Delta_{0\,K}{}^{T}S_m^\circ$, $\Delta_{0\,K}{}^{T}H_m^\circ$, and Φ_m° are the heat capacity, standard entropy, standard enthalpy, and Gibbs function, respectively. Nuclear contributions were excluded when calculating thermodynamic functions. Values are reported with extended significant digits to preserve the original measurement precision and facilitate future data fitting and modeling.

clearly indicates the (expected) occurrence of incongruent vaporization, confirming the impossibility to deposit a thin film of $BaZrS_3$ from the bulk powder, at least under near-equilibrium conditions.

Partial pressures of neutral species in the vapor were estimated by means of eq 1. Note that measured ion intensities of Ba-containing species showed a contribution from thermal ionization which was subtracted to obtain the electron impact signal I_k^+ to be used in eq 1. Ionization cross sections were taken from ref 41. The so-evaluated partial pressures of gaseous species released by $BaZrS_3$ at the various temperatures for the three experiments are reported in Tables S3−S5, in chronological order. It is evident from these values that the composition of the gas phase changes continuously with time for a given temperature, thus indicating that a monovariant heterogeneous equilibrium inside the cell is not attained, as also suggested by the already mentioned variation of sulfur activity as a function of time and temperature (Figure S4).

In order to verify if BaS(s) was formed upon decomposition of the $BaZrS_3$, its activity was estimated from the ratio of BaS

https://doi.org/10.1021/acs.jpcc.6c01064
J. Phys. Chem. C 2026, 130, 7153−7166

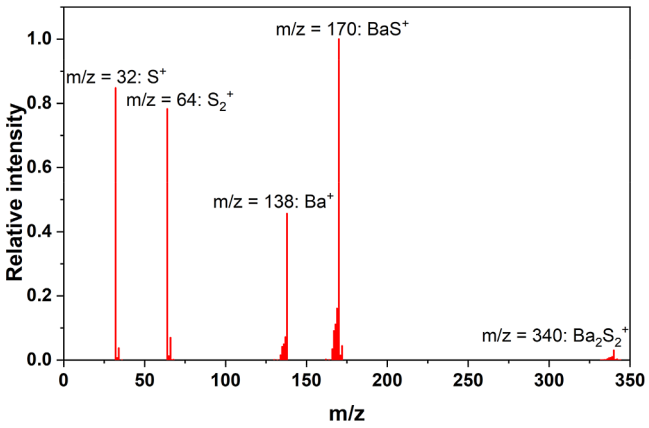

Figure 2. Mass spectrum of the vapor phase above $BaZrS_3$ at T = 1829 K.

partial pressures measured via $BaZrS_3$ vaporization and those obtained in a separate experiment on pure BaS (see Figure S5), $a_{BaS} = \frac{p_{BaS}^{BaZrS_3}}{p_{BaS}^{BaS}}$. The comparison between partial pressures of BaS in the $BaZrS_3$ and those of pure BaS is shown in Figure 3. As

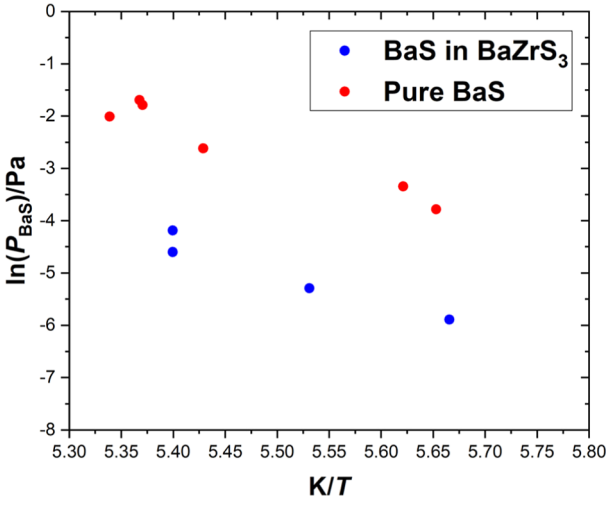

Figure 3. BaS partial pressure *vs* reciprocal temperature for $BaZrS_3$ and for pure BaS.

can be inferred from the comparison of partial pressures, the values of BaS activity in the $BaZrS_3$ (ranging from 0.10 to 0.12) point to the absence of pure BaS(s) in the solid phase formed by thermal decomposition of $BaZrS_3$.

In order to attempt the identification of the decomposition process(es) occurring during heating and to determine whether there is a chemical interaction between the sample and the crucible material, the residual sample of KEMS experiments was subject to PXRD, SEM, TEM and Raman analyses. PXRD patterns were acquired after each KEMS run, whereas SEM and TEM and Raman spectra were performed on the final residue only. The PXRD patterns in Figure S6 display, besides the peaks of residual $BaZrS_3$, a number of new peaks whose intensities gradually increase from the first to the third residue. However, the only Ba−Zr−S phase that could be unambiguously assigned was the 2D Ruddlesden−Popper Ba_2ZrS_4 phase. Stoichiometric considerations could suggest the simultaneous formation of a Zr−S binary phase. Nevertheless, the remaining peaks in the residue are not clearly attributable to any known zirconium sulfide pattern. This made it impossible to identify any heterogeneous equilibrium established in the effusion cell and to derive the corresponding thermodynamic properties. The presence of tungsten-containing phases that could form from possible interaction with the crucible material was ruled out. Note that the absence of pure BaS in the PXRD pattern seems to confirm the low activity of BaS in the solid phase, consistently with the BaS(g) partial pressure data discussed above. Based on Raman spectra of the residue sample (see here below) the formation of ZrO_2 in nanocrystalline form (not detected in PXRD patterns) is suggested.

TEM and SEM analysis of KEMS residue compared with those of pristine sample revealed a higher degree of crystallinity in the former, due to high temperature crystallization, evidenced by a more ordered disposition of lattice planes in TEM images of the residue and a more regular shape of the grains in SEM images of the same sample, as can be seen in Figure 4a−d.

Electron diffraction obtained by TEM from polycrystalline pristine $BaZrS_3$ confirmed phase purity, in agreement with SEM−EDX analysis (Table S6). Conversely, analysis of the KEMS residue identified only the residual $BaZrS_3$ and 2D Ruddlesden−Popper Ba_2ZrS_4 among the possible binary and ternary phases.

The presence of Ba_2ZrS_4 is confirmed by its electron-diffraction pattern (Figure S7), which matches the reference pattern.[42] This finding is also consistent with the PXRD data of the residue and is in reasonable agreement with the SEM−EDX analysis (Table S7). The sulfur abundance determined by EDX (46% at.) could be a slight underestimation or could be affected by other unidentified sulfur-poor phases.

Raman spectra of the residue, performed with excitation wavelength of 633 and 785 nm (Figure 5a,b), revealed the presence of a few phases produced after KEMS experiments. In particular, none of the spectra, performed on various spots of the sample as indicated by numbers 1−3 in the figures, resemble that of $BaZrS_3$.[28] ZrO_2, possibly formed as a nanocrystalline phase (and therefore difficult to see through XRD) by reaction promoted at high temperature by the residual oxygen partial pressure in the vacuum environment of the KEMS instrument, was identified in at least one spot with the use of 633 nm laser. Notably, the combination of spectra of spots 1 and 2 performed with 633 nm laser roughly gives the spectrum of spot 3, supporting the presence of Ba_2ZrS_4 and ZrO_2 phases, the former identified by comparison with the spectrum reported by Ishii et al.[43] Similarly, Raman spectra performed with 785 nm laser do not match the reference spectrum of $BaZrS_3$[28] nor that of $Ba_3Zr_2S_7$ reported by Ishii et al.,[43] while confirming once again the presence of Ba_2ZrS_4, in agreement with the previously discussed analysis, in the spot 2. The existence of Ba_2ZrS_4, possibly together with an unidentified phase, is also suggested by the spectra, very similar to each other, of spots 1 and 3 performed using 785 nm laser.

Finally, we used the measured partial pressures to determine the enthalpy change of the isomolecular gas phase equilibrium

$$BaS(g) + S(g) \rightleftarrows Ba(g) + S_2(g) \quad (6)$$

and, from there, the enthalpy of dissociation (bond enthalpy) at 0 K of BaS(g). Note that this reaction has the advantage of being independent of the instrumental constant in eq 1, k_{instr},

https://doi.org/10.1021/acs.jpcc.6c01064
J. Phys. Chem. C 2026, 130, 7153−7166

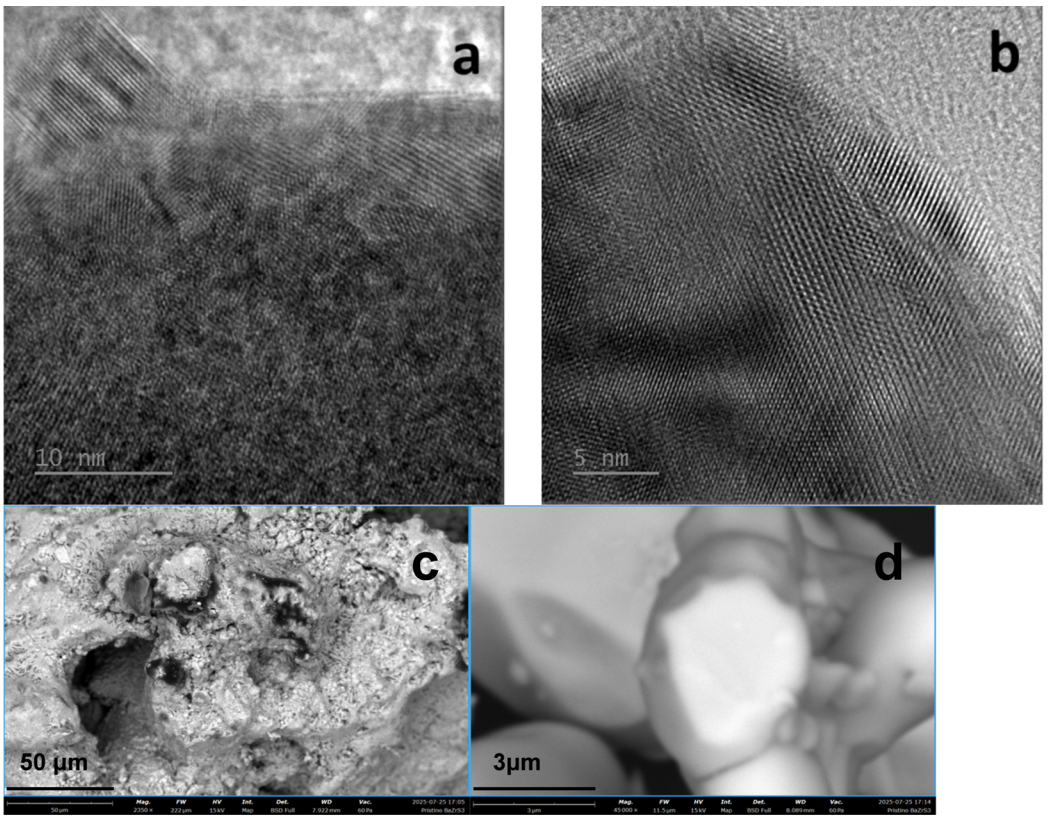

Figure 4. TEM images of (a) pristine $BaZrS_3$ and (b) residue from KEMS experiments, and SEM images of (c) pristine and (d) KEMS residue.

and therefore is not affected by possible uncertainties in determination of its value.

The $\Delta_r H_{0K}^\circ$ of reaction (6) was obtained by applying the so-called third-law method of analysis of vapor pressure data[44]

$$\Delta_r H_{0K}^\circ = -RT\ln K_{eq} + T(\Delta\Phi_T^\circ) \quad (7)$$

where Φ_T° is defined as

$$\Phi_T^\circ = -\frac{G_T^\circ - H_{0K}^\circ}{T} \quad (8)$$

The free energy functions of the various species were taken from the IVTANTHERMO thermochemical database.[45] The $\Delta_r H_{0K}^\circ$ of reaction (6) obtained for different temperatures are shown in Table 6.

From these values, a mean $\Delta_r H_{0K}^\circ = (-27.2 \pm 0.6)$ kJ·mol^{-1} was obtained, which in turn yielded a dissociation enthalpy of BaS(g) of (393.4 ± 20.6) kJ·mol^{-1}. This value is in good agreement with the only previously reported determination,[46] $\Delta_r H_{0K}^\circ = (396.2 \pm 18.8)$ kJ·mol^{-1}.

3.3. Intrinsic and Extrinsic Thermodynamic Stability of $BaZrS_3$ and $BaHfS_3$

The absolute entropies derived from measured heat capacities of $BaZrS_3$ and $BaHfS_3$ enable to estimate the Gibbs energy of formation of the two compounds, as well as to perform some thermodynamic predictions on their stability in different conditions and environments.

To the best of our knowledge, no experimental value of the enthalpy of formation from elements ($\Delta_f H^\circ$) of $BaZrS_3$ and $BaHfS_3$ is available in the literature. Our attempts to estimate these quantities from high-temperature decomposition processes were unsuccessful because no well-defined heterogeneous equilibrium was established. In the past few years, however, a number of computational studies have reported the energy of formation of both perovskites from their binary precursors

$$BaS(s) + MS_2(s) \rightarrow BaMS_3(s)(\text{with M} = \text{Hf, Zr}) \quad (9)$$

A summary of these theoretical values is given in Table 7. The mean values are −33.4 kJ·mol^{-1} for $BaZrS_3$ and −33.9 kJ·mol^{-1} for $BaHfS_3$, respectively. To convert these values to the corresponding enthalpy changes at 0 K, the zero point energy and the small $P\Delta V$ term should, in principle, be considered. However, for the purpose of estimating thermodynamic stability, on first approximation these contributions can be neglected. Conversion of the enthalpy difference from 0 to 298 K would require the heat contents of all precursors. Because the heat contents of ZrS_2 and HfS_2 are undetermined, this contribution to $\Delta_r H_{298K}^\circ$ of reactions (eq 9) was also neglected. This approximation is the rough equivalent of assuming additivity of heat capacity values at low temperature (i.e., the Kopp-Neumann rule).

As for the entropy change at 298 K of reactions in eq 9, it was evaluated by using the absolute entropies of $BaHfS_3$ and $BaZrS_3$ in Tables 4 and 5, respectively, the value 78.45 J·K^{-1}·mol^{-1} for BaS[45] and the estimated values of 78.2 and 83.7 J·K^{-1}·mol^{-1} for ZrS_2[47] and HfS_2,[48] respectively. The absolute entropies of the two chalcogenide perovskite phases resulted thus to be higher than the sum of the absolute entropies of the binary sulfide precursors BaS and ZrS_2 or HfS_2, at least within the limits of accuracy of the latter, which are only available as empirical estimates. The resulting entropy changes for reactions in eq 9 are 16.8 J·K^{-1}·mol^{-1} for $BaZrS_3$ and 20.7 J·K^{-1}·mol^{-1} for $BaHfS_3$. The increases in entropy imply that the thermodynamic stability of both perovskites relative to binary

https://doi.org/10.1021/acs.jpcc.6c01064
J. Phys. Chem. C 2026, 130, 7153−7166

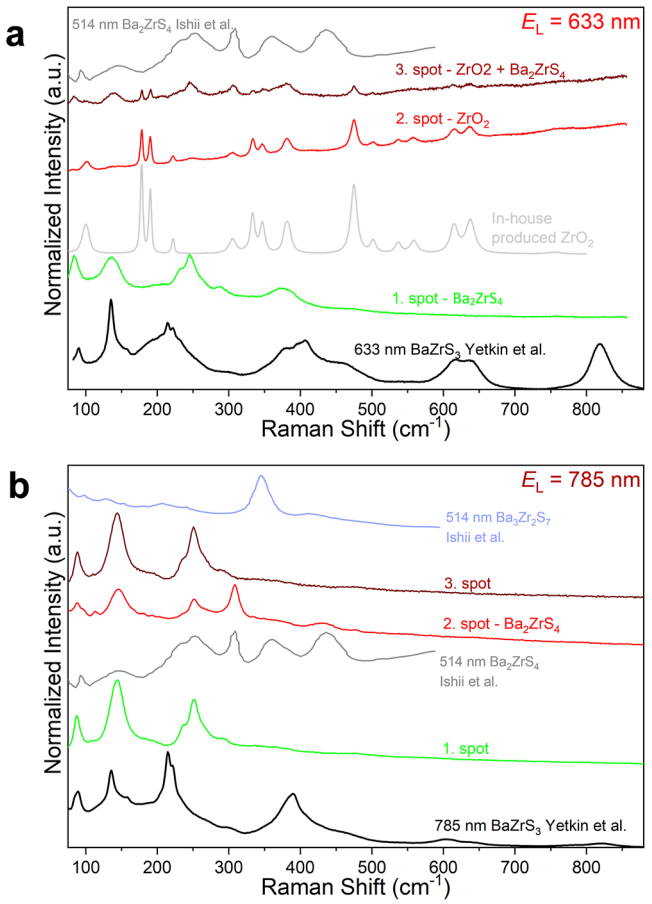

Figure 5. Raman spectra performed on various spots (indicated by numbers 1−3) of the solid residue obtained after KEMS experiments at (a) 633 nm and (b) 785 nm excitation wavelength. Reference spectra of $BaZrS_3$ from ref 28 and of Ruddlesden−Popper phases from ref 43 are shown for comparison.

Table 6. Standard Reaction Enthalpy at 0 K of (6) Obtained by Third-Law Treatment of KEMS Data

T/K	$\Delta_r H_{0K}°$/kJ·mol^{-1}
1808	−26.73
1852	−27.81
1852	−27.03

Table 7. Energy of Formation (in kJ·mol^{-1}) from Binary Sulfide Precursors (eq 9) for $BaZrS_3$ and $BaHfS_3$ from Computational Works and Online Repositories[a]

$BaZrS_3$	$BaHfS_3$
−27.9;[14] −38.5;[15] −21.3;[16] −44.0;[18] −32.7;[19] −38.5;[20] −30.6;[21] −33.8[22]	−40.3;[14] −28.9;[17] −42.0;[18] −28.0;[21] −30.1[22]

[a]References are indicated as superscript next to the values.

sulfides increases with temperature. This trend is in agreement with first-principles lattice dynamics calculations.[26]

The above-described procedure leads us to propose the following estimates for the change in Gibbs energy of reaction (eq 9)

$$\Delta_r G°(9)(BaZrS_3) = (-33.4 - 16.8\cdot10^{-3}T/K)\text{kJ·mol}^{-1} \quad (10)$$

$$\Delta_r G°(9)(BaHfS_3) = (-33.9 - 20.7\cdot10^{-3}T/K)\text{kJ·mol}^{-1} \quad (11)$$

The $\Delta_r G°$ at 298 K calculated from eqs 10 and 11 are, respectively, −38.5 kJ·mol^{-1} for $BaZrS_3$ and −40.1 kJ·mol^{-1} for $BaHfS_3$, indicating that both compounds are thermodynamically stable with respect to binary precursors. The only literature value available for comparison is the computational result of −50 kJ·mol^{-1} by Kayastha et al.[26] for $BaZrS_3$, which would indicate a slightly higher stability. Outside of possible inaccuracies in the computational results, uncertainties in eqs 10 and 11 may arise from the estimated entropies of the binary phases. It should be also noted that the $\Delta_r H°$ and $\Delta_r S°$ values used in eqs 10 and 11 are those at 298 K, with no temperature dependence included, due to the lack of heat capacity data for the perovskite phases at higher temperature.

From eqs 10 and 11 we determine the corresponding expressions for the formation reactions from the elements

$$Ba(s) + M(s) + 3S(s) \rightarrow BaMS_3(s) \text{ (with M = Hf, Zr)} \quad (12)$$

using literature enthalpies of formation for the binary sulfides, $\Delta_f H°(BaS)$ = −470 kJ·mol^{-1},[45] $\Delta_f H°(ZrS_2)$ = −573 kJ·mol^{-1},[47] and $\Delta_f H°(HfS_2)$ = −575 kJ·mol^{-1}.[48] The formation entropies were derived by combining the absolute entropies of perovskites measured in this work with absolute entropies of elements at 298 K. The resulting expressions are the following

$$\Delta_r G°(12)(BaZrS_3) = (-1077 + 24.3\cdot10^{-3}T/K)\text{kJ·mol}^{-1} \quad (13)$$

$$\Delta_r G°(12)(BaHfS_3) = (-1079 + 19.3\cdot10^{-3}T/K)\text{kJ·mol}^{-1} \quad (14)$$

These expressions are valid near 298 K within the uncertainties of the enthalpic and entropic terms.

The corresponding formation enthalpy values are −1077 kJ·mol^{-1} for $BaZrS_3$ and −1079 kJ·mol^{-1} for $BaHfS_3$. For $BaZrS_3$, this value compares well with the theoretical value of −1052 kJ·mol^{-1} reported in ref 26. A similar level of agreement is found for the Gibbs energy of formation at 298 K (−1070 kJ·mol^{-1} in this work and −1037 kJ·mol^{-1} in ref 26). Unlike the formation from binary sulfides, the formation of both perovskites from the elements becomes less favorable with increasing temperature, although $\Delta_f G°$ remains strongly negative over several hundred kelvins.

Using the resulting $\Delta_f G°$ values, we evaluated the extrinsic thermodynamic stability of both compounds by considering a number of potential decomposition reactions in the presence of oxygen, water, and water + CO_2. Again, all the thermodynamic quantities for the species involved in these reactions were taken from IVTANTHERMO database.[45] Reactions considered in this evaluation of stability and the corresponding $\Delta_r G°$ at 298 K are listed in Table 8. Note that we did not consider BaO as a possible product of oxidation in reactions (1) to (5), due to the low stability of this oxide compared to ZrO_2 and HfO_2. This assumption was also validated by the equilibrium calculations reported below.

As can be seen from the values in Table 8, all the reactions with oxygen at 298 K are extremely favored from a thermodynamic point of view. Reaction with water and CO_2 is also favored at the reference temperature, although $\Delta_r G°$ is much less negative, compared with reactions with oxygen. The very negative $\Delta_r G°$ of reactions of $BaZrS_3$ and $BaHfS_3$ with

https://doi.org/10.1021/acs.jpcc.6c01064
J. Phys. Chem. C 2026, 130, 7153−7166

Table 8. Gibbs Energy (in kJ·mol^{-1}) and ln K_p at T = 298 K of Possible Decomposition Reactions of $BaZrS_3$ and $BaHfS_3$

	reaction	$\Delta_rG°$ 298 K (M = Zr)	ln (K_p 298 K) (M = Zr)	$\Delta_rG°$ 298 K (M = Hf)	ln (K_p 298 K) (M = Hf)
1	$BaMS_3(s) + 3O_2(g) \rightleftarrows BaS(s) + MO_2(s) + 2SO_2(g)$	−1035	417.9	−1040	419.5
2	$BaMS_3(s) + 7/2O_2(g) \rightleftarrows BaSO_4(s) + MO_2(s) + S_2O(g)$	−1415	571.1	−1419	572.7
3	$BaMS_3(s) + 4O_2(g) \rightleftarrows BaSO_4(s) + MO_2(s) + 2SO(g)$	−1371	553.5	−1376	555.2
4	$BaMS_3(s) + 5O_2(g) \rightleftarrows BaSO_4(s) + MO_2(s) + 2SO_2(g)$	−1929	778.6	−1933	780.2
5	$BaMS_3(s) + 6O_2(g) \rightleftarrows BaSO_4(s) + MO_2(s) + 2SO_3(g)$	−2071	835.9	−2075	837.5
6	$BaMS_3(s) + 4H_2O(l) \rightleftarrows Ba(OH)_2(s) + MO_2(s) + 3H_2S(g)$	24.40	−9.847	20.36	−8.219
7	$BaMS_3(s) + 3H_2O(l) + CO_2(g) \rightleftarrows BaCO_3(s) + MO_2(s) + 3H_2S(g)$	−99.90	40.32	−103.9	41.95

oxygen may appear surprising, considering that experiments show long-term stability of both compounds at ambient atmosphere.[49] The observed stability is most likely due to a very high kinetic barrier that hinders decomposition under typical storage conditions. Among the selected decomposition processes, only reaction with water is not favored thermodynamically at 298 K according to reaction 6 in Table 8. In a recent paper, $BaZrS_3$ was found to decompose in aqueous environments due to sulfur oxidation.[50] However, additional thermodynamic driving force under these conditions could be due to the formation of ionic species, not considered in reaction 6. Interestingly, theoretical calculations in ref 50 indicate that sulfur loss from perovskite can hardly be energetically explained by the formation of sulfur vacancies, and an important role of O_2 adsorption is suggested instead. Indeed, we calculate for the $\Delta_rG°$of reaction $BaZrS_3(s) + 2H_2O(l) + 2O_2(g) \rightleftarrows ZrO_2(s) + BaSO_4(s) + 2H_2S(g)$ a value of −1292 kJ·mol^{-1}, which indicate a clear thermodynamic enhancement of sulfur oxidation in the presence of oxygen.

As regards the first reaction reported in Table 8 for $BaZrS_3$, an interesting comparison can be made with the work by Bystrický et al.:[51] based on thermogravimetric analysis, these authors propose this process as the first of a two-step mechanism of decomposition of the perovskite at high temperature, and they give $\Delta_rH°$ = −1090 kJ·mol^{-1}, in very good agreement with our estimate of −1084 kJ·mol^{-1}.

Finally, from the $\Delta_rS°$of these decomposition reactions, it was also possible to evaluate their temperature dependence, as shown in Figure 6a,b.

As shown in Figure 6, while all the reactions with oxygen are more thermodynamically favored (more negative $\Delta_rG°$) at low temperature, reactions with water become favored with increasing temperature. Finally, the decomposition process with water and CO_2, having a slightly negative $\Delta_rG°$ at low temperature, becomes more and more favored with increasing temperature.

The standard Gibbs energy changes discussed above provide a rather clear idea of the thermodynamic tendency toward degradation. However, the most direct method to investigate the thermodynamically driven degradation paths is based on the prediction of the final (equilibrium) conditions, as provided by the nature and composition of the phases resulting from decomposition, attained from the material under given initial conditions. To this end, we performed a number of equilibrium calculations by using the Gibbs energy minimization module POLY-3 of the Thermo-Calc software package (see Section 2.8 for details) to gain more insight into the degradation behavior of $BaZrS_3$.

The starting conditions were selected to test the material stability (i) under atmospheric and reduced oxygen pressure; (ii) at room temperature, at a plausible operation temperature

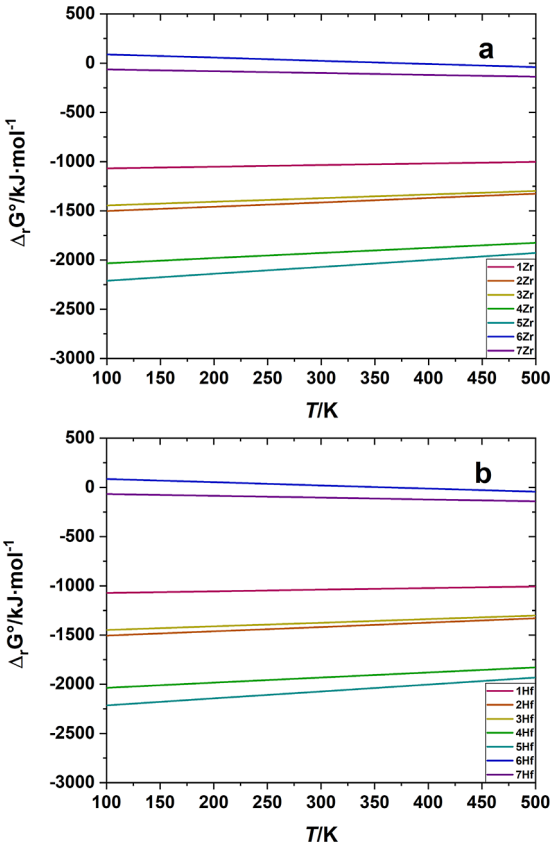

Figure 6. Temperature dependence of $\Delta_rG°$ of reactions in Table 8 for (a) $BaZrS_3$ and (b) $BaHfS_3$. The symbols 1Zr, 2Zr etc. refer to the reaction number in the table.

under intense heating from the Sun (350 K), and at 500 K as a harsher thermal condition; (iii) under saturated water pressure and 400 ppm for CO_2. The selected conditions are reported in Table 9 together with the set of solid phases formed at equilibrium and the composition of the produced gas phase. Only the most abundant species are reported for the latter. As can be easily seen, barium sulfate, zirconium oxide, and barium sulfide are the solid phases whose formation is thermodynamically favored under most conditions, whereas the formation of zirconium sulfide seems not to occur. However, it should be remembered that the phase identification and the thermodynamic description of Zr−S phases is far from being complete and the only phases included in the database are ZrS_2 and Zr_2S_3. Even more important, no ternary Ba−Zr−S phase, except $BaZrS_3$, is included in the database, due to the complete lack of thermodynamic information on 2D phases. This limitation seems particularly severe in view of the results presented in Section 3.2. On the other hand, the formation of

https://doi.org/10.1021/acs.jpcc.6c01064
J. Phys. Chem. C 2026, 130, 7153−7166

Table 9. Thermodynamic Degradation Pattern of $BaZrS_3$ under Selected Reactive Atmospheres at 298, 350, and 500 K[b]

298 K						350 K						500 K					
Initial conditions			Equilibrium conditions			Initial conditions			Equilibrium conditions			Initial conditions			Equilibrium conditions		
pO_2	pH_2O	pCO_2	Cond. phases[a]	Gas (x_i)	p tot	pO_2	pH_2O	pCO_2	Cond. phases[a]	Gas (x_i)	p tot	pO_2	pH_2O	pCO_2	Cond. phases[a]	Gas (x_i)	p tot
21000	-	-	$BaSO_4$, $BaZrS_3$, ZrO_2, S	S_8 (0.77), S_6 (0.21), S_7 (0.018)	$3.58\cdot10^{-4}$	21000	-	-	$BaSO_4$, $BaZrS_3$, ZrO_2,S	S_8 (0.76), S_6 (0.21), S_7 (0.033)	0.152	21000	-	-	$BaSO_4$, $BaZrS_3$, ZrO_2,S (liquid)	S_8 (0.63), S_6 (0.27), S_7 (0.1)	938
100	-	-	$BaSO_4$, $BaZrS_3$, ZrO_2, S	S_8 (0.77), S_6 (0.21), S_7 (0.018)	$3.58\cdot10^{-4}$	100	-	-	$BaSO_4$, $BaZrS_3$, ZrO_2,S	S_8 (0.76), S_6 (0.21), S_7 (0.033)	0.152	100	-	-	$BaSO_4$, BaS, $BaZrS_3$, ZrO_2	S_6 (0.51), S_8 (0.35), S_7 (0.011)	13.3
-	3132	-	$BaSO_4$, $BaZrS_3$, ZrO_2	H_2S (≈1)	3122	-	47373	-	BaS, $BaZrS_3$, ZrO_2	H_2S (0.9996),H_2O ($3.4\cdot10^{-4}$), H_2 ($2.4\cdot10^{-5}$)	47434	-	2645000	-	BaS, $BaZrS_3$, ZrO_2	H_2S (0.992), H_2O ($5.7\cdot10^{-3}$), H_2S_2 ($1.7\cdot10^{-3}$)	2640000
-	100	-	$BaSO_4$, $BaZrS_3$, ZrO_2	H_2S (≈1)	100	-	100	-	$BaSO_4$, $BaZrS_3$, ZrO_2	H_2S (0.998), S_8 ($1.1\cdot10^{-3}$), S_6 ($3.2\cdot10^{-4}$)	100	-	100	-	$BaZrS_3$, ZrO_2	H_2S (0.999), H_2 ($5.9\cdot10^{-4}$), H_2S_2 ($4.0\cdot10^{-4}$)	99.8
-	3132	40	$BaCO_3$, BaS, $BaZrS_3$, ZrO_2	H_2S (0.99), CH_4 ($5.2\cdot10^{-3}$), H_2O ($5.6\cdot10^{-5}$)	3118	-	47373	40	$BaCO_3$, BaS, $BaZrS_3$, ZrO_2	H_2S (0.999), H_2O ($3.4\cdot10^{-4}$), H_2S_2 ($5.5\cdot10^{-5}$)	47434	-	2645000	40	BaS, $BaZrS_3$, ZrO_2	H_2S (0.992), H_2O ($5.7\cdot10^{-3}$), H_2S_2 ($2.1\cdot10^{-3}$)	2640000

[a]Note that the formation of ternary Ba−Zr−S phases other than $BaZrS_3$ cannot occur in the simulation, because no 2D ternary phases are included in the database owing to the lack of any thermodynamic data. [b]All Pressures are Given in Pa.

https://doi.org/10.1021/acs.jpcc.6c01064
J. Phys. Chem. C 2026, 130, 7153−7166

$Ba(OH)_2$ under saturated water environment is not thermodynamically allowed. As expected, in the presence of CO_2 (at the typical atmospheric concentration), barium carbonate is preferentially formed. With regard to the equilibrated vapor phase, hydrogen sulfide is the main degradation product, both under $H_2O(g)$ and under $H_2O(g)$ + $CO_2(g)$ atmospheres. Interestingly, the largely prevailing species in the gas phase produced under an oxygen atmosphere are the homonuclear sulfur oligomers, with no significant presence of sulfur oxides in the explored temperature range.

4. CONCLUSIONS

Absolute entropies and other thermodynamic properties of chalcogenide perovskites $BaZrS_3$ and $BaHfS_3$ have been determined for the first time by measuring isobaric heat capacity from 1.8 to 300 K. Additionally, thermal degradation of the $BaZrS_3$ perovskite was investigated in the temperature range 462−1852 K under effusion conditions, and the gas species released from decomposition were identified by mass spectrometry. The vapor phase was found to contain only sulfur, as S(g) and $S_2(g)$ species, up to about 1600 K, while, above this temperature, the species Ba(g), BaS(g) and $Ba_2S_2(g)$ were also observed in the mass spectrum. The activities of sulfur and BaS were estimated as a function of temperature and the dissociation energy of BaS(g) was determined. XRD diffraction patterns, TEM, SEM−EDX and Raman analyses performed on the residual samples of KEMS experiments revealed the formation of the Ruddlesden−Popper phase Ba_2ZrS_4, confirming previous theoretical predictions. However, no isothermal invariance of pressures was observed, making it impossible to perform a thermodynamic analysis of partial pressure data.

By combining the absolute entropies determined in this work with energies of formation retrieved from previous computational works, it was possible to estimate the Gibbs energy of formation of the two perovskites both from binary sulfide precursors and from the elements and to evaluate their stability in various conditions. Both $BaZrS_3$ and $BaHfS_3$ were shown to be stable with respect to the binary sulfides BaS, ZrS_2 and HfS_2 at room temperature, with the entropic term causing further stabilization at higher temperatures. Reaction with oxygen is extremely favored at room temperature from a thermodynamic point of view, yielding barium sulfate and zirconium oxide, although oxidation is not observed experimentally, most probably due to kinetic hindrance. The same products are formed under water + oxygen atmosphere, whereas barium carbonate is formed under water + carbon dioxide atmosphere.

■ ASSOCIATED CONTENT

Supporting Information

The Supporting Information is available free of charge at https://pubs.acs.org/doi/10.1021/acs.jpcc.6c01064.

Powder diffraction patterns of the as-prepared $BaZrS_3$ and $BaHfS_3$ with reference patterns (Figure S1); thermogravimetric curves of $BaZrS_3$ and $BaHfS_3$ before and after heat treatment in high vacuum (Figure S2); molar heat capacities measured for $BaHfS_3$ and $BaZrS_3$ (Tables S1 and S2); deviation plots of the heat capacity results from the theoretical fits for $BaHfS_3$ and $BaZrS_3$ (Figure S3); sulfur activity as a function of time and temperature in KEMS experiments on $BaZrS_3$ (Figure S4); mass spectrum of the vapor phase above BaS (Figure S5); partial pressures of gaseous species released by $BaZrS_3$ in KEMS experiments (Tables S3−S5); XRD pattern of the as-prepared $BaZrS_3$ and of solid residues of the same sample after KEMS experiments (Figure S6); experimental Ba_2ZrS_4 electron diffraction pattern overlapped to the reference one (Figure S7); results of SEM−EDX analysis on the as-prepared $BaZrS_3$ and on the solid residue after KEMS experiments (Tables S6−S7) (PDF)

■ AUTHOR INFORMATION

Corresponding Authors

Andrea Ciccioli − *Department of Chemistry, Sapienza University of Rome, Rome 00185, Italy;* orcid.org/0000-0003-1421-8062; Email: andrea.ciccioli@uniroma1.it

Brian Woodfield − *Department of Chemistry and Biochemistry, Brigham Young University, Provo, Utah 84602-2401, United States*; Email: bfwoodfield@chem.byu.edu

Lorenza Romagnoli − *Department of Chemistry, Sapienza University of Rome, Rome 00185, Italy;* orcid.org/0009-0007-6628-1684; Email: lorenza.romagnoli@uniroma1.it

Authors

Alexis Gibson − *Department of Chemistry and Biochemistry, Brigham Young University, Provo, Utah 84602-2401, United States*

Natalie Parkinson − *Department of Chemistry and Biochemistry, Brigham Young University, Provo, Utah 84602-2401, United States*

Riccardo Testa − *Department of Chemistry, Sapienza University of Rome, Rome 00185, Italy;* orcid.org/0009-0007-5711-4382

Corrado Di Conzo − *Department of Applied Science and Technology (DISAT), Polytechnic of Turin, Turin 10129, Italy; Department of Basic and Applied Sciences for Engineering (SBAI), Sapienza University of Rome, Rome 00161, Italy*

Marco Rossi − *Department of Basic and Applied Sciences for Engineering (SBAI), Sapienza University of Rome, Rome 00161, Italy; Research Centre for Nanotechnology Applied to Engineering (CNIS), Sapienza University of Rome, Rome 00185, Italy*

Alessandro Latini − *Department of Chemistry, Sapienza University of Rome, Rome 00185, Italy;* orcid.org/0000-0002-3205-4826

Stefano Vecchio Cipriotti − *Department of Basic and Applied Sciences for Engineering (SBAI), Sapienza University of Rome, Rome 00161, Italy;* orcid.org/0000-0002-7864-4266

Hasan Arif Yetkin − *Department of Physics and Materials Science, University of Luxembourg, Belvaux 4422, Luxembourg*

Phillip J. Dale − *Department of Physics and Materials Science, University of Luxembourg, Belvaux 4422, Luxembourg*

Complete contact information is available at: https://pubs.acs.org/10.1021/acs.jpcc.6c01064

Notes

The authors declare no competing financial interest.

https://doi.org/10.1021/acs.jpcc.6c01064
J. Phys. Chem. C 2026, 130, 7153−7166

■ ACKNOWLEDGMENTS

This study was carried out within the NEST—Network for Energy Sustainable Transition and received funding from the European Union Next-GenerationEU (PIANO NAZIONALE DI RIPRESA E RESILIENZA (PNRR)—MISSIONE 4 COMPONENTE 2, INVESTIMENTO 1.3). This manuscript reflects only the authors' views and opinions, neither the European Union nor the European Commission can be considered responsible for them. This work was also partially funded within the project "Ricerche di Ateneo, Sapienza University of Rome—Synthesis and physicochemical characterization of chalcogenide perovskites for photovoltaic applications", grant no. RM123188F7BADB03 (PI Andrea Ciccioli). This article is also based upon the work from COST Action RenewPV CA21148, supported by COST (European Cooperation in Science and Technology).

■ REFERENCES

(1) Sun, Y.-Y.; Agiorgousis, M. L.; Zhang, P.; Zhang, S. Chalcogenide Perovskites for Photovoltaics. *Nano Lett.* **2015**, *15*, 581−585.
(2) Sopiha, K. V.; Comparotto, C.; Márquez, J. A.; Scragg, J. J. S. Chalcogenide Perovskites: Tantalizing Prospects, Challenging Materials. *Adv. Opt. Mater.* **2022**, *10*, 2101704.
(3) Chowdhury, T. A.; Bin Zafar, M. A.; Sajjad-Ul Islam, M.; Shahinuzzaman, M.; Islam, M. A.; Khandaker, M. U. Stability of perovskite solar cells: issues and prospects. *RSC Adv.* **2023**, *13*, 1787−1810.
(4) Grinberg, I.; West, D. W.; Torres, M.; Gou, G.; Stein, D. M.; Wu, L.; Chen, G.; Gallo, E. M.; Akbashev, A. R.; Davies, P. K.; Spanier, J. E.; Rappe, A. M. Perovskite oxides for visible-light-absorbing ferroelectric and photovoltaic materials. *Nature* **2013**, *503*, 509−512.
(5) Bhalla, A.; Guo, R.; Roy, R. The perovskite structure − a review of its role in ceramic science and technology. *Mater. Res. Innov.* **2000**, *4*, 3−26.
(6) Peña, M. A.; Fierro, J. L. G. Chemical Structures and Performance of Perovskite Oxides. *Chem. Rev.* **2001**, *101*, 1981−2017.
(7) Grabowska, E. Selected perovskite oxides: Characterization, preparation and photocatalytic properties—A review. *Appl. Catal. B Environ.* **2016**, *186*, 97−126.
(8) Shockley, W.; Queisser, H. J. Detailed Balance Limit of Efficiency of p-n Junction Solar Cells. *J. Appl. Phys.* **1961**, *32*, 510−519.
(9) Hahn, H.; Mutschke, U. UntersuchungenüberternäreChalkogenide, Zur XI. Versuche zur Darstellung von Thioperowskiten. *Z. Anorg. Allg. Chem.* **1957**, *288*, 269−278.
(10) Clearfield, A. The Synthesis and Crystal Structures of some Alkaline Earth Titanium and Zirconium Sulfides. *Acta Crystallogr.* **1963**, *16*, 135−142.
(11) Lelieveld, R.; Ijdo, D. J. W. Sulphides with the $GdFeO_3$ Structure. *Acta Crystallogr., Sect. A:* **1980**, *B36*, 2223−2226.
(12) Agarwal, S.; Vincent, K. C.; Agrawal, R. From synthesis to application: a review of $BaZrS_3$ chalcogenide perovskites. *Nanoscale* **2025**, *17*, 4250−4300.
(13) Ju, M.-G.; Dai, J.; Ma, L.; Zeng, X. C. Perovskite Chalcogenides with Optimal Bandgap and Desired Optical Absorption for Photovoltaic Devices. *Adv. Energy Mater.* **2017**, *7*, 1700216.
(14) Chami, R.; Lekdadri, A.; Omari, L. H.; Hlil, E. K.; Chafi, M. Investigation of the photovoltaic properties of $BaHf_{1-x}Zr_xS_3$ ($x \leq 1$) chalcogenide perovskites using first principles calculations. *Mater. Today Energy* **2021**, *20*, 100689.
(15) Liu, D.; Zeng, H.; Peng, H.; Sa, R. Computational study of the fundamentalproperties of Zr-based chalcogenide perovskites for optoelectronics. *Phys. Chem. Chem. Phys.* **2023**, *25*, 13755−13765.
(16) Meng, W.; Saparov, B.; Hong, F.; Wang, F.; Mitzi, D. B.; Yan, Y. Alloying and Defect Control within Chalcogenide Perovskitesfor Optimized Photovoltaic Application. *Chem. Mater.* **2016**, *28*, 821−829.
(17) Sun, Q.; Yin, W. J. Thermodynamic Stability Trend of Cubic Perovskites. *J. Am. Chem. Soc.* **2017**, *139*, 14905−14908.
(18) Filippone, S. A.; Sun, Y. Y.; Jaramillo, R. The effect of animproved density functional on the thermodynamics and adsorption-controlled growth windows of chalcogenide perovskites. *MRS Adv.* **2018**, *3*, 3249−3254.
(19) Huo, Z.; Wei, S.-H.; Yin, W.-J. High-throughput screening of chalcogenide single perovskites by first-principles calculations for photovoltaics. *J. Phys. D: Appl. Phys.* **2018**, *51*, 474003.
(20) Zhang, P.; Chen, B.; Zhu, W.; Wang, C.; Zhang, W.; Li, Y.; Liu, W. First-principles prediction of structural, mechanical and thermal properties of perovskite $BaZrS_3$. *Eur. Phys. J. B* **2020**, *93*, 97.
(21) Jain, A.; Ong, S. P.; Hautier, G.; Chen, W.; Richards, W. D.; Dacek, S.; Cholia, S.; Gunter, D.; Skinner, D.; Ceder, G.; Persson, K. A. Commentary: The Materials Project: A materials genomeapproach to accelerating materials innovation. *APL Mater.* **2013**, *1*, 011002.
(22) Saal, J. E.; Kirklin, S.; Aykol, M.; Meredig, B.; Wolverton, C. Materials Design and Discovery with High-Throughput Density Functional Theory: The Open Quantum Materials Database (OQMD). *JOM* **2013**, *65*, 1501−1509.
(23) Kirklin, S.; Saal, J. E.; Meredig, B.; Thompson, A.; Doak, J. W.; Aykol, M.; Rühl, S.; Wolverton, C. The Open Quantum Materials Database (OQMD): assessing the accuracy of DFT formation energies. *npj Comput. Mater.* **2015**, *1*, 15010.
(24) Kayastha, P.; Tiwari, D.; Holland, A.; Hutter, O. S.; Durose, K.; Whalley, L. D.; Longo, G. High-Temperature Equilibrium of 3D and 2D ChalcogenidePerovskites. *Sol. RRL* **2023**, *7*, 2201078.
(25) Jackson, A. J.; Walsh, A. *Ab initio* thermodynamic model of Cu_2ZnSnS_4. *J. Mater. Chem. A* **2014**, *2*, 7829−7836.
(26) Kayastha, P.; Longo, G.; Whalley, L. D. A First-Principles Thermodynamic Model for the Ba−Zr−S System in Equilibrium with Sulfur Vapor. *ACS Appl. Energy Mater.* **2024**, *7*, 11326−11333.
(27) Romagnoli, L.; Ciccioli, A.; Dale, P. J.; Yetkin, H. A.; Panetta, R.; Latini, A. A simple synthetic approach to $BaZrS_3$, $BaHfS_3$, and their solid solutions. *J. Am. Ceram. Soc.* **2024**, *107*, 698−703.
(28) Yetkin, H. A.; Dale, P. J.; Kshirsagar, A. R.; Reichardt, S.; Redinger, A.; Latini, A.; Ciccioli, A.; Romagnoli, L. A Combined Theoretical and Experimental Raman Scattering Study of BaZrS3−BaHfS3 Solid Solutions. *ChemPhysChem* **2024**, *25*, No. e202400340.
(29) Shi, Q.; Boerio-Goates, J.; Woodfield, B. F. An Improved Technique for Accurate Heat Capacity Measurements on Powdered Samples Using a Commercial Relaxation Calorimeter. *J. Chem. Thermodyn.* **2011**, *43*, 1263−1269.
(30) Shi, Q.; Snow, C. L.; Boerio-Goates, J.; Woodfield, B. F. Accurate Heat Capacity Measurements on Powdered Samples Using a Quantum Design Physical Property Measurement System. *J. Chem. Thermodyn.* **2010**, *42*, 1107−1115.
(31) Pesci, M.; Romagnoli, L.; Brunetti, B.; Vecchio Ciprioti, S.; Ciccioli, A.; Latini, A. Stability of Tin-Containing Hybrid Perovskites: The Thermal Decomposition of Formamidinium Tin Triiodide ($FASnI_3$) Investigated by Thermogravimetry and Effusion Techniques. *J. Phys. Chem. C* **2025**, *129*, 9291−9301.
(32) Kiser, R. W. *Introduction to Mass Spectrometry and Its Applications*; Kansas State University, Manhattan, Prentice-Hall, Inc.: Englewood Cliffs, NJ, 1965.
(33) Angeletti, L.; Agostini, M.; Figueira, B. A. M.; Latini, A.; Paris, E. C.; De Giorgio, F.; Schultz, T.; Di Conzo, C.; Mura, F.; Rossi, M.; Yadav, N. G.; Adelhelm, P.; Mazzei, F.; Brutti, S.; Quaranta, S. A sustainable δ-MnO_2 derived from Amazon rainforest Mn-ore tailings for applications in lithium-ion batteries. *Sustain. Mater. Technol.* **2025**, *44*, No. e01347.
(34) Klinger, M.; Polívka, L.; Jager, A.; Tyunina, M. Quantitative analysis of structural inhomogeneity in nanomaterials using transmission electron microscopy. *J. Appl. Crystallogr.* **2016**, *49*, 762−770.
(35) *ThermoCalc Software Package*, version L, 1997. https://thermocalc.com (accessed March 31, 2026).

https://doi.org/10.1021/acs.jpcc.6c01064
J. Phys. Chem. C 2026, 130, 7153−7166

(36) *SGTE substances database (SUB94)*. https://www.sgte.net/en/sgte-substance-sgsub (accessed March 31, 2026).
(37) Gopal, E. S. R. *Specific Heats at Low Temperatures*; Plenum Press: New York, 1966.
(38) Sundström, L. J. Low Temperature Heat Capacity of the Rare Earth Metals. *Handb. Phys. Chem. Rare Earths* **1978**, *1*, 379−410.
(39) Justice, B. H. *Thermal Data Fitting with Orthogonal Functions and Combined Table Generation*; The FITAB Program: United States Medium, 1969.
(40) Rosen, P. F.; Woodfield, B. F. Standard Methods for Heat Capacity Measurements on a Quantum Design Physical Property Measurement System. *J. Chem. Thermodyn.* **2020**, *141*, 105974.
(41) Drowart, J.; Chatillon, C.; Hastie, J.; Bonnell, D. High-Temperature Mass Spectrometry: Instrumental Techniques, Ionization Cross-Sections, Pressure Measurements, and Thermodynamic Data. *Pure Appl. Chem.* **2005**, *77*, 683−737.
(42) Chen, B.-H.; Eichhorn, B. Synthesis and structure of two new Ba_2MS_4 phases where M = Zr,Hf: a new series of K_2NiF_4solids. *Mater. Res. Bull.* **1991**, *26*, 1035−1040.
(43) Ishii, M.; Saeki, M.; Sekita, M. Vibrational spectra of barium-zirconium sulfides. *Mater. Res. Bull.* **1993**, *28*, 493−500.
(44) Romagnoli, L.; Almeida, A. R. R. P.; Silva Ferraz, J. M.; Latini, A.; Freitas, V. L. S.; Ribeiro da Silva, M. D. M. C.; Schiavi, P. G.; Vecchio Ciprioti, S.; Ciccioli, A. Thermodynamic study of tin tetraiodide (SnI_4) sublimation by effusion techniques. *J. Chem. Thermodyn.* **2024**, *199*, 107348.
(45) Iorish, V. S. *IVTANTHERMO database*. Version 3.0, Glushko Thermocenter of Russian Academy of Sciences, 2005.
(46) Colin, R.; Goldfinger, P.; Jeunehomme, J. Mass-spectrometric studies of the vaporization of sulphides of calcium, strontium and barium. The dissociation Energy of S_2 and SO. *Trans. Faraday Soc.* **1964**, *60*, 306−316.
(47) Brown, P. L.; Curti, E.; Grambow, B.; Ekberg, C.; Mompean, F. J.; Perrone, J. *Chemical Thermodynamics of Zirconium*; OECD Nuclear Energy Agency: Data Bank, Issy-les-Moulineaux (France), (2005).
(48) Fiechter, S.; Eckert, K. Crystal growth of HfS_2 by chemical vapour transport with halogen (Cl, Br, I). *J. Cryst. Growth* **1988**, *88*, 435−441.
(49) Perera, S.; Hui, H.; Zhao, C.; Xue, H.; Sun, F.; Deng, C.; Gross, N.; Milleville, C.; Xu, X.; Watson, D. F.; Weinstein, B.; Sun, Y.-Y.; Zhang, S.; Zeng, H. Chalcogenide perovskites − an emerging class of ionic semiconductors. *Nano Energy* **2016**, *22*, 129−135.
(50) Meng, J.; Lan, Z. Aqueous Instability of the Chalcogenide Perovskite $BaZrS_3$. *Nano Lett.* **2026**, *26*, 197−204.
(51) Bystrický, R.; Tiwari, S. K.; Hutár, P.; Sýkora, M. Thermal Stability of Chalcogenide Perovskites. *Inorg. Chem.* **2024**, *63*, 12826−12838.

https://doi.org/10.1021/acs.jpcc.6c01064
J. Phys. Chem. C 2026, 130, 7153−7166